

Controlling the Role of Nanopore Morphology in Capillary Condensation

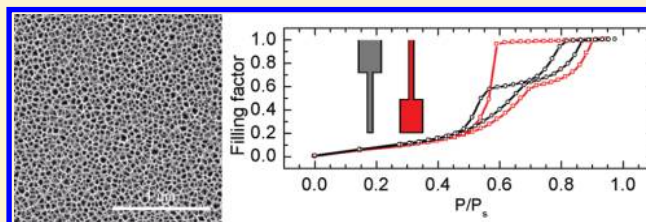
Fèlix Casanova,^{*,†,§,||} Casey E. Chiang,^{†,‡} Anne M. Ruminski,[‡] Michael J. Sailor,[‡] and Ivan K. Schuller[†]

[†]Physics Department and [‡]Department of Chemistry and Biochemistry, University of California—San Diego, La Jolla, California 92093, United States

[§]CIC nanoGUNE, 20018 Donostia-San Sebastian, Basque Country, Spain

^{||}IKERBASQUE, Basque Foundation for Science, 48011 Bilbao, Basque Country, Spain

ABSTRACT: The effect of pore morphology on capillary condensation and evaporation in nanoporous silicon is studied experimentally. A variety of cooperative and local effects are observed in tailored nanopores with well-defined regions by directly probing gas adsorption in each region using optical interferometry. All observations are ascribed to the ability of the nanopore region to access the gas reservoir directly and the nucleation of liquid bridges at local heterogeneities within the nanopore region. These assumptions, consistent with recent simulations, can be extended to any real nanoporous system.



1. INTRODUCTION

Nanoporous materials have many promising properties that can be used both in applications (biosensing,¹ chemical sensing,² and nanotemplates³) and fundamental studies (e.g., phase transitions in confined geometries⁴). They come in a variety of shapes and sizes, ranging from disordered/interconnected porous materials such as oxide xerogels⁵ or Vycor glass⁶ to regular networks such as SBA-16⁷ or even well-defined, disconnected cylindrical pores such as porous alumina^{8–10} or MCM-41.¹¹ For optimal use of these materials, information about the pore morphology (internal surface structure) and topology (connectivity) is essential. A commonly used technique for pore characterization is sorption analysis, in which the sorption isotherm (i.e., the constant-temperature relationship between vapor adsorbed/desorbed and the relative vapor pressure) is used to generate information regarding the pore size distribution and pore connectivity.¹²

To characterize pores using sorption analysis, it is crucial to understand how pore morphology affects sorption. Although this is well understood for the simplest cases (i.e., disconnected cylindrical pores^{8–11}), deviation from ideality drastically affects the quantitative correlation between pore morphology and sorption isotherms.^{13,14} Although large size variations within the pores affect capillary condensation and evaporation,¹⁵ recent simulations suggest that small perturbations^{16–21} have a larger effect than previously considered. This uncertainty requires further investigation into the mechanisms behind capillary condensation and evaporation in real systems.²² A clear example is the long-standing controversy regarding the correlation between the pore morphology and hysteresis shape in single-crystal porous silicon (Si).^{14,18,22,23}

Previous experimental^{15,23–27} and theoretical^{13,28,29} studies have shown that complex geometries create cooperative effects that alter capillary condensation and evaporation within a

nanoporous medium. For an “ink-bottle” geometry in which a narrow pore (“constriction”) constricts a wider pore (“cavity”), there is experimental evidence of cavitation^{23,26} within single-crystal porous Si and pore-blocking in various other nanoporous media.^{15,24,27} For a “funnel” geometry (cavity above constriction), there is one experimental observation of advanced adsorption,²⁴ as predicted theoretically by Cordero et al.^{13,28}

In this work, we use optical interferometry to investigate how a particular porous region is affected by the presence of a morphologically different one. Two morphologically different porous regions were combined to produce two complex structures (ink bottle and funnel) as well as two single structures (one composed solely of cavities and the other of constrictions). Multiple configurations enable the separation of cooperative effects (due to different pore morphology between pore regions) from local effects (within a pore region), thus giving insight into the global behavior of capillary condensation and evaporation in inhomogeneous pores.

2. EXPERIMENTAL SECTION

2.1. Fabrication. A set of four porous Si samples was fabricated by combining electrochemical etches of high and low currents in aqueous ethanolic HF (3:1 v/v 49% aqueous HF/ethanol) to produce layers composed of pores with nanometer-sized diameters (Figure 1a).¹ In this manner, an artificial junction was created at a specific depth that joined regions with two very different morphologies (Figure 1b). All samples were fabricated from single-crystal highly doped p-type silicon (0.00125 Ω cm resistivity, (100) polished, B-doped). To prevent a surface crust layer that may form on etched p⁺⁺ silicon, a sacrificial etch of 462 mA cm⁻² for 15 s was performed first on all samples and

Received: December 14, 2011

Revised: March 23, 2012

Published: April 10, 2012

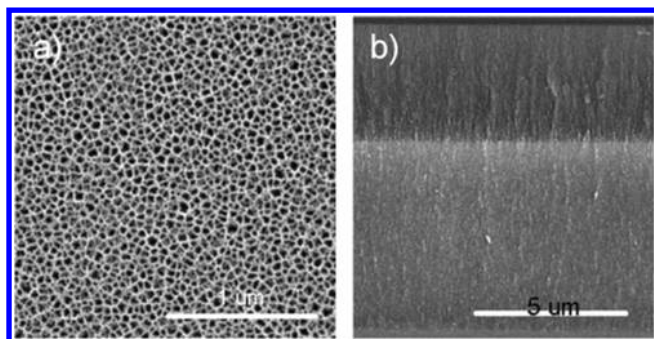


Figure 1. (a) Top-view SEM image of pSi1 and (b) cross-sectional SEM image of pSi1 showing layers of two distinct porosities.

removed with dilute basic KOH in water and ethanol.³⁰ The first sample was fabricated by applying a current density of 462 mA cm^{-2} for 15 s, followed by a current density of 77 mA cm^{-2} for 120 s, resulting in a structure with cavities above constrictions (pSi1, funnel). For the second sample, the current was applied in the reverse order, with 77 mA cm^{-2} for 120 s being followed by 462 mA cm^{-2} for 15 s such that a structure with constrictions above cavities was fabricated (pSi2, ink bottle). Finally, single layers were also fabricated by applying only the lower current density (pSi3, isolated constriction) or the higher current density (pSi4, isolated cavity). All samples were used without further postanodization treatment.

Depletion of the fluoride ion can lead to variations in porosity and pore size with depth during the electrochemical etching of porous Si.³⁰ For this study, the samples were prepared using relatively high concentrations of HF that were mixed during etching to avoid this possibility. Although we saw no evidence of the variation in pore dimensions with depth by electron microscopy, we cannot rule out that slight variations in pore size with depth exist in these samples. When preparing double-layer structures, the HF solution was replaced before etching the second layer. Again, the HF solution was mixed during etching to encourage effective acid refreshment.

The porosity ρ (which is directly related to the pore morphology) and pore length L were obtained by using optical interferometry and applying the two-component Bruggeman effective medium approximation¹ to empty and liquid-filled pores; these data are summarized in Table 1.

Table 1. Porosity ρ and Length L of As-Etched Porous Silicon Layers

sample id	$\rho_{\text{layer 1}}$ (%)	$L_{\text{layer 1}}$ (μm)	$\rho_{\text{layer 2}}$ (%)	$L_{\text{layer 2}}$ (μm)	geometry
pSi1	69.4	3.341	54.0	5.949	funnel
pSi2	54.0	5.862	69.7	3.226	ink bottle
pSi3	53.6	5.839	N/A	N/A	isolated constriction
pSi4	68.9	3.400	N/A	N/A	isolated cavity

The excellent reproducibility of ρ and L for the same etching conditions, regardless of the position of the layer ($\rho \approx 69\%$ and $L \approx 3.3 \mu\text{m}$ are prepared using high current density and $\rho \approx 54\%$ and $L \approx 5.9 \mu\text{m}$ are prepared using low current density) strongly suggests consistent pore size formation and enables a direct comparison of the complex structures to their constituents. Top-view and cross-sectional scanning electron microscopy (SEM) images show that, for the small pores, average pore diameters are less than 10 nm (below the resolution of the SEM) and $54 \pm 20 \text{ nm}$ for the large ones. The SEM measurements confirm that individual pores have a polygonal shape¹⁴ (Figure 1a), with a pore texture predominantly oriented perpendicular to the substrate (Figure 1b), as expected for pores in (100)-oriented p-type Si.³¹

2.2. Optical Analysis. Reflectance spectra were obtained using a tungsten white light source together with a spectrometer, based on a

linear CCD array, in a 90° backscattering configuration, as previously described.^{1,24} For pore diameters much smaller than the probing wavelengths, as in our case, the sample can be considered to be a single medium with an effective refractive index of n_{eff} that can be modeled by the Bruggeman effective medium approximation.¹ The spectra

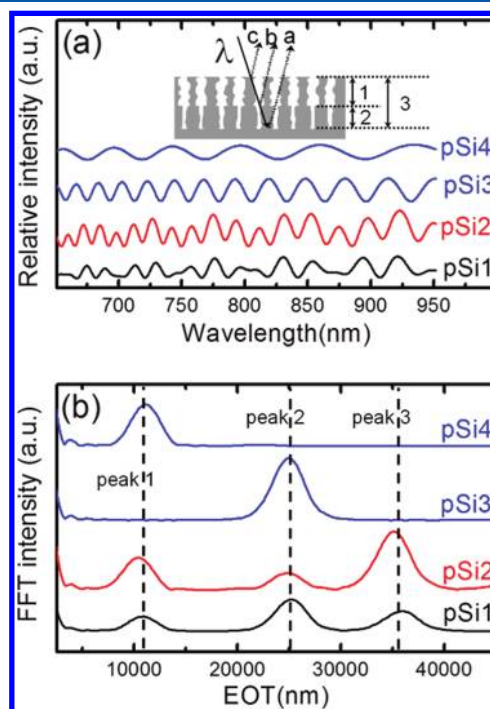


Figure 2. (a) Reflectance spectra for each of the four samples: pSi1 (funnel) and pSi2 (ink bottle) double porous layers show a combination of multiple frequencies whereas pSi3 (isolated constriction) and pSi4 (isolated cavity) single porous layers show pure frequencies arising from interference only at the top and bottom interfaces. (Inset) Schematic illustrating where the multiple frequencies are generated in a double layer. Interference between reflected light at a and b monitor the bottom layer, b and c, the top layer, and a and c, the entire sample. (b) Fast Fourier transforms showing the effective optical thicknesses (EOTs) extracted from the reflectance spectra in a. Peak 1 (11 000 nm) corresponds to the cavities, peak 2 (25 000 nm), to the constrictions, and peak 3 (36 000 nm), to the entire sample.

display a complex series of fringes (Figure 2a), which result from the interference of the light beams reflected at each interface (inset in Figure 2a). A simple treatment by McLeod³² adequately models the interference relationship for a double layer, where the reflectance R of light is given by

$$R \propto A \cos(\delta_1) + B \cos(\delta_2) + C \cos(\delta_1 + \delta_2) \quad (1)$$

with $\delta_i = 2n_{\text{eff},i}L_i k$ for each layer ($i = 1, 2$), where $k = 2\pi/\lambda$ is the wavenumber. A , B , and C are constants related to the light intensity and index contrast between layers.¹ A single layer can be described by a single refractive index, leaving only one term in eq 1.

A fast Fourier transform (FFT) of a reflectance spectrum R yields peaks (Figure 2b) whose positions correspond to $2n_{\text{eff},i}L_i$, which is the effective optical thickness (EOT) of the porous layer(s).²⁴ Note that in order to perform an FFT, R must be plotted versus k instead of versus λ , which is how data were acquired in Figure 2a. Equation 1 implies that the EOT associated with the third peak should be equal to the sum of the EOT for each individual layer, which indeed is confirmed by the sum of peaks 1 and 2, giving peak 3 (Figure 2b). By using the measured EOT, ρ , and L from Table 1 and literature values for the refractive indices of silicon, hexane, and nitrogen ($n_{\text{Si}} = 3.72$, $n_{\text{hexane}} =$

1.37, and $n_{N_2} = 1.00$) in the three-component Bruggeman approximation³³

$$(1 - \rho) \frac{(n_{Si}^2 - n_{eff}^2)}{(n_{Si}^2 + 2n_{eff}^2)} + (1 - f)\rho \frac{(n_{N_2}^2 - n_{eff}^2)}{(n_{N_2}^2 + 2n_{eff}^2)} + f\rho \frac{(n_{hexane}^2 - n_{eff}^2)}{(n_{hexane}^2 + 2n_{eff}^2)} = 0 \quad (2)$$

we obtain f , the dimensionless filling factor. In this work, f is the fraction of hexane within the pore volume of a specific layer, defined to be 0 for the empty pores and 1 for the liquid-filled pores.

2.3. Measurement. Gas dosing was performed in a 2 cm³ Teflon sample cell fitted with a glass window. Saturated hexane vapor was generated by bubbling pure N₂ through liquid hexane at 25 °C and then diluted by mixing the effluent with pure N₂ using a computer-controlled gas dosing system. Relative vapor pressures, P/P_s (where P_s is the saturation vapor pressure), were calculated using the dilution ratio of the gas dosing system. For the measurement, P/P_s was increased from zero to saturation and then decreased back to zero in a stepwise fashion, remaining at each interval for a duration long enough to allow for equilibration at each step¹⁰ (3 min in the present case). However, it is possible that, because of the extremely slow relaxation of uptake in the hysteresis region, a true equilibrium is not reached and the measurement represents a local minimum in the free energy.⁶ The real-time acquisition of reflectance spectra during dosing enabled us to obtain f simultaneously for each specific layer within a sample, thus generating sorption isotherms for each independent layer.

3. RESULTS

The optical measurement allows us to extract sorption isotherm data from individual layers in either the funnel (sample pSi1) or the ink-bottle (sample pSi2) structure. The ink-bottle structure contains a layer of small pores (constrictions) on top of a layer of larger pores (cavities), and the funnel structure contains a layer of large pores (cavities) on top of a layer of smaller pores (constrictions). Because the Fourier transform of the optical spectrum separates the individual layers into individual spectral peaks (Figure 2b), it is relatively simple to identify condensation processes occurring in each layer and in the structure as a whole.²⁴ Thus, Figure 3a shows adsorption data for the entire structure, Figure 3b displays data from the layer containing just the cavity portion of the structure, and Figure 3c displays the data from the layer containing the constrictions. We note again that the sum of the isotherms for the individual layers is equal to the isotherm for the full structure. For comparison, data from samples containing only a single layer of constrictions (sample pSi3) or only a single layer of cavities (sample pSi4) are also presented in Figure 3.

4. DISCUSSION

With increasing P/P_s , there are three distinct mechanisms associated with the sorption isotherm: multilayer adsorption on the walls, capillary condensation, and the disappearance of the liquid–vapor interface (i.e., meniscus) following capillary condensation. When P/P_s is decreased from its maximal value of 1, the operative processes are as follows: meniscus formation followed by capillary evaporation and finally multilayer desorption from the walls.¹² We will focus our discussion on the hysteretic region in which capillary condensation and evaporation occur, as it is related to the confinement of hexane, and can thus be used to characterize the internal pore morphology.

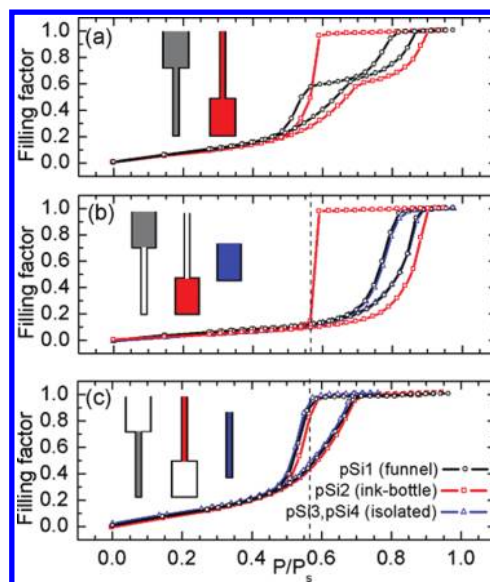


Figure 3. Sorption isotherms for the four sample structures showing the hexane fraction within the pore volume (filling factor, f) as a function of the relative vapor pressure (P/P_s) at 25 °C for (a) the entire sample, (b) the cavities, and (c) the constrictions. Error bars are smaller than the size of the symbols. The black curves were generated from pSi1 (funnel), the red, from pSi2 (ink bottle), and the blue, from pSi3 and pSi4 (single layers). The insets in each graph indicate the layer being monitored by each sorption isotherm. The responses from these individual layers are extracted from the optical interference spectrum as described in the text.

Capillary condensation and evaporation occurs at a relative vapor pressure described by the Kelvin equation¹² (eq 3), which for a concave meniscus takes the form of

$$\ln\left(\frac{P}{P_s}\right) = -\frac{2\gamma V_L}{RT r_m} \quad (3)$$

where r_m is the radius of curvature for the meniscus, R is the ideal gas constant, and V_L and γ are the molar volume and surface tension of the liquid at temperature T . Equation 3 implies that capillary condensation and evaporation directly probe the radius of curvature of the meniscus formed at the pore, providing valuable information about the pore morphology. Through a detailed examination of the initial capillary condensation event and subsequent evaporation from our four samples, we propose a model that explains the behavior of capillary condensation and evaporation observed within our porous Si structures.

4.1. Condensation. Capillary condensation is marked by a sharp change in f upon a small increase in P/P_s . Figure 3a shows that capillary condensation in the ink bottle (pSi2, red squares) is slightly delayed (requires larger P/P_s) with respect to capillary condensation in the funnel (pSi1, black circles) and that condensation occurs in two discrete and sequential steps for both structures. We can gain insight into the capillary condensation mechanism as it relates to pore morphology by analyzing the sorption isotherms for each pore region and comparing them to the isotherms of the isolated constituents (pSi3 and pSi4).

4.1.1. Cavities. First, we compare the condensation in the cavities of the ink bottle (pSi2) with the isolated case (pSi4). Figure 3b shows that capillary condensation within the cavity layer is delayed in the ink-bottle case (pSi2, red squares). From

Figure 3c, we know that the constriction layer in the ink-bottle structure (pSi2, red squares) is liquid-filled at lower P/P_s , which precludes direct access of the cavity to the gas reservoir, in contrast to the isolated cavity (pSi4), which has direct access to the gas reservoir. Similar to previous studies in ink-bottle geometries,^{23,24} capillary condensation still occurs within the cavity, but in this case it occurs at a different and slightly higher P/P_s than in the isolated case. It is also worth noting that the amount of adsorbed analyte in the cavities of the ink bottle (pSi2) before condensation is lower than in the isolated cavities, even at P/P_s below the onset of condensation of the isolated pore (pSi4), as observed in Figure 3b.

The same delay has recently been reported in tailored ink-bottle porous silicon,²⁶ although no explanation was given for this behavior. This is very different from what was observed in nearly ideal porous alumina,²⁴ in which advanced adsorption¹³ (the equilibrium advance of the meniscus formed by condensation in the constriction) with respect to the isolated case occurs. Although an interpretation of these behaviors is given in section 4.3, they already suggest that the nucleation mechanism for condensation in porous silicon is different from an ideal case. Such a suggestion is supported by our examination of the other geometries.

In the funnel geometry (pSi1), the cavity is in direct contact with the gas reservoir, so any shift in the condensation pressure is attributable to interactions with the adjacent constriction. The data (Figure 3) show that all condensation has occurred within the constriction (black circles in Figure 3c), thus creating a hemispherical meniscus. The capillary condensation within the cavity remains identical to that observed from pSi4 (i.e., the isolated cavity; black circles and blue triangles in Figure 3b, respectively). This may arise from either of two situations: (1) capillary condensation within the cavity can either be nucleated at the cavity end by the meniscus (created either by condensation within an adjacent constriction¹³ (pSi1, funnel) or by multilayer adsorption at the capped end³⁴ (pSi4, isolated cavity)) or (2) physical and/or chemical heterogeneities within the cavity itself nucleate the gas–liquid phase transition, as was suggested experimentally by Wallacher²³ and investigated recently by numerical simulations.^{13,16–21} Capillary condensation within the cavities of the ink bottle (see above) and constrictions (see below) confirms the latter to be the case.

4.1.2. Constrictions. Figure 3c shows that the isotherms for the constrictions are identical for all three configurations: at the top (pSi2, ink-bottle sample), at the bottom (pSi1, funnel sample), or as an isolated (pSi3) porous region. The lack of cooperative effects can be explained by the fact that these regions always have direct access to the gas reservoir prior to the gas–liquid phase transition as predicted by eq 3. However, the identical occurrence of capillary condensation in all three samples irrespective of their pore ending is in direct contrast to the classical Cohan model,^{12,34} which predicts that, in ideal cylindrical pores, capped pores (constriction at the bottom of the funnel sample, pSi1, and isolated constriction, pSi3) and pores open at both ends (constriction at the top of the ink-bottle sample, pSi2) should condense at different pressures because of the presence or absence of a pre-existing meniscus. In the former case, the radius of curvature of the meniscus is expected to arise from nucleation of a hemispherical meniscus at the capped end, whereas in the latter case it comes from the curvature of the wall (cylindrical meniscus), leading to a meniscus radius of curvature that differs by a factor of 2 when one considers the two different geometries.^{12,34} The lack of

influence of the pore ends, also observed in other work,^{14,23} strongly suggests that porous Si possesses a substantial degree of disorder.

Furthermore and also in agreement with previous results in porous Si,¹⁴ capillary condensation in the pores with direct access to the gas reservoir occurs at a P/P_s that is lower than what the Cohan model would predict for condensation both for a cylindrical meniscus and for a hemispherical meniscus, when using the pore sizes determined by SEM images in the Cohan model calculation. This could not be checked for the constrictions in pSi1 (funnel), pSi2 (ink bottle), and pSi3 (isolated) because we were unable to resolve the pore size with our SEM measurements. However, it is clearly observed for the cavities in pSi1 (funnel) and pSi4 (isolated), which contain pore diameters of 54 ± 20 nm. These latter samples yield a calculated value of P/P_s of ~ 0.93 for capillary condensation (considering the Kelvin equation with a hemispherical meniscus), which is significantly larger than the measured P/P_s value of ~ 0.85 .

Both observations (i.e., the lack of influence of the pore ends and the condensation at a P/P_s lower than predicted by the ideal case of a hemispherical meniscus) can be explained by considering that the condensation and growth of liquid bridges occur where the pore width is smallest.¹⁸ On the basis of these and previous (section 4.1.1) observations, we conclude that within pores with significant amounts of disorder (i.e., porous Si) it is not the boundary conditions but rather local heterogeneities in the microstructure that are most relevant in determining the capillary condensation. This conclusion is supported and in general agreement with other authors.^{17–19,23}

4.2. Evaporation. We now focus on the evaporation process. Figure 3a shows that liquid in the funnel sample (pSi1, black circles) evaporates in two distinct events, whereas liquid in the ink-bottle sample (pSi2, red squares) evaporates in a single event that is sharp at the beginning and more gradual at the end. An examination of the optical data, which allows for the extraction of the individual isotherms for each layer, identifies which feature (cavity or constriction) is responsible for the global behavior seen in Figure 3a.

4.2.1. Cavities. Starting with the cavities (Figure 3b), the liquid–gas phase transition is drastically altered if there is surviving liquid above (ink bottle, pSi2, red squares) the region of interest and seemingly unperturbed otherwise (funnel, pSi1, black circles). A comparison with the isolated regions (blue triangles) in Figure 3b,c shows that liquid remains the stable phase in the constrictions to lower P/P_s than in the cavities. Therefore, in the ink-bottle sample (pSi2), there is still liquid in the constriction separating the liquid-filled cavity from the gas reservoir at a value of P/P_s for which evaporation is expected to occur from an unobstructed cavity. This liquid prohibits evaporation at the same P/P_s for which evaporation is observed in the sample that does not contain a bottleneck over the cavity. This is the classical pore-blocking effect¹² that generally governs capillary evaporation from ink-bottle geometries. These results are similar to those observed with porous alumina^{24,27} and porous Si using Ar at 63.5 K²³ but in direct contrast to other studies of porous Si in which cavitation is observed.^{23,26} The discrepancy can be attributed to the different relative pore sizes as well as the different temperatures and analytes used in the various studies because it is known that the occurrence of pore blocking or cavitation depends on the relative stability of the liquids confined at the constriction and at the cavity.²¹ Thus, it is again observed that a liquid region connecting the external

gas reservoir to the cavity has a significant impact upon the phase transition within the cavity. The cavities (red squares in Figure 3b) and constrictions (red squares in Figure 3c) in the ink-bottle sample (pSi2) indicate that the fast but delayed evaporation in pSi2 (red squares in Figure 3a) is due to the complete emptying of the cavities. This occurs after the beginning but prior to the completion of the emptying of the constrictions (dashed lines in Figures 3b,c), an intermediate situation between classical pore blocking and cavitation.³⁵ A similar observation has been recently reported in tailored ink-bottle porous Si²⁶ using Ar at 60 K, in contrast to the porous alumina case.²⁴ This is probably due to the different morphological properties of porous alumina (nearly ideal geometry) and porous Si (with local microstructural heterogeneities).

4.2.2. Constrictions and Cavities with Free Access to the Gas Reservoir. We now discuss the case in which the adjacent region does not obstruct the gas reservoir (i.e., the cavity in funnel sample pSi1 (black circles in Figure 3b) and the constrictions in funnel sample pSi1 and ink-bottle sample pSi2 (black circles and red squares in Figure 3c, respectively)). The desorption branch lies on top of the isolated case (blue triangles in Figure 3b,c) for all configurations, consistent with our assumption that the presence of a gas-filled adjacent region does not affect the meniscus that should govern capillary evaporation. This indicates that, for the ink-bottle sample (pSi2), evaporation from the cavity through the constriction does not alter evaporation within the constriction.

During desorption, we again find that it is direct access to the gas reservoir that dictates evaporation. The Kelvin equation implies that the condensate should evaporate from the wider pores before evaporating from the narrow pores. This leads to the expected identical liquid evaporation in the cavities of funnel sample pSi1 and isolated pSi4. It also produces identical evaporation in the constrictions of funnel pSi1, ink-bottle pSi2, and isolated pSi3 samples. In all of these cases, pore emptying is the same regardless of the boundary conditions, supporting the idea that local heterogeneities control capillary evaporation.

4.3. Model. A simple model consistent with the previous observations is based on assumptions derived from two factors: nucleation by local heterogeneities and access to the gas reservoir.

On one hand, the nucleation in an isolated pore is controlled by local heterogeneities. Condensation occurs first in narrower areas, creating liquid bridges that grow and fill the pore before the prediction from the Kelvin equation. This mechanism, observed in recent simulations,^{16–19,21} is not affected by boundary conditions (pores open at one or both ends or a preformed meniscus in an adjacent region).^{16,19}

On the other hand, the ability to access the gas reservoir directly is what determines capillary condensation and evaporation. During multilayer adsorption, both cavities and constrictions have equal access to the gas reservoir and thus behave identically to the isolated pore. If the pore region is not blocked by liquid prior to the expected behavior of the isolated pore, then liquid analyte will condense/evaporate at the same pressure as for the isolated pore, as observed in cavities of pSi1 (funnel) and pSi4 (isolated) and constrictions of pSi1 (funnel), pSi2 (ink-bottle), and pSi3 (isolated). If the cavity is blocked by condensation at the constriction (ink-bottle geometry, pSi2), then local heterogeneities in the cavity cannot play a role. In this case, condensation will be governed by the existing hemispherical meniscus at the constriction (delayed with

respect to the isolated case), and the evaporation will be determined by pore-blocking and/or cavitation effects (again delayed with respect to the isolated case).

Although the effect of pore blocking on evaporation has been widely reported in the literature,^{12,21,23,26,27} the same effect on condensation has been less frequently discussed. Ideally, the gas phase in the blocked cavity is at equilibrium with the gas reservoir, and condensation occurs by advanced adsorption of the meniscus formed at the interface with the blocking constriction,¹³ as has been observed in porous alumina ink bottles.²⁴ However, in the case of porous Si (unlike porous alumina), adsorption is dominated by the many metastable states created by the disorder present in the pores.¹⁸ This is known to slow the transient dynamics of adsorption.^{6,18} We observe that, in the blocked cavities, the amount of adsorbed analyte is lower than in the isolated cavities for the same relative pressures and that capillary condensation occurs at higher relative pressures. The same experimental observation is reported in ref 26. Although a definitive explanation cannot be made at this time, we anticipate that it might be explained by considering that, in the blocked cavities, the dynamics associated with this particular local minimum in the free-energy landscape are slower than in the isolated cavities. Because the equilibration time used for the measurement of the adsorption isotherms is the same, the cavities in the ink-bottle system are not fully at equilibrium with the external gas reservoir, and the advance of the hemispherical meniscus of the constrictions toward the cavities takes place before the local inhomogeneities of the cavities can nucleate the liquid bridges.

Surprisingly, this suggests that capillary condensation in the blocked part of a complex pore provides the most accurate pore size distribution, perhaps even more accurate than its single-layered constituent. The reason is that the isolated pore, unblocked, has a likelihood of condensation being nucleated by heterogeneities, which causes an underestimation of the average pore diameter (section 4.1.2). On the contrary, in a blocked pore region, heterogeneities are inaccessible to the gas reservoir and condensation will occur from the advanced adsorption of the hemispherical meniscus created at the boundary with the filled (blocking) region. In this case, condensation will follow the Kelvin equation corresponding to the real pore diameter. As an example, condensation in the cavity of pSi2 (ink-bottle) together with the Kelvin equation for a hemispherical meniscus implies a pore diameter of ~ 40 nm, close to that in the SEM images (54 ± 20 nm). However, the pore diameter calculated for condensation in the cavity of the pSi1 (funnel) or pSi4 (isolated cavity) structures is ~ 25 nm.

Finally, we should stress that the large-scale cavity-constriction structures we have created reproduce basic cooperative effects (pore blocking, cavitation, and advanced adsorption) that ultimately explain the behavior on the local scale (in which the heterogeneities can be seen as chains of cavities and constrictions).

5. CONCLUSIONS

We have successfully used a combination of fabrication and interferometric techniques to deliberately tailor complex pore structures in porous silicon and locally measure capillary condensation and evaporation, which can be quantitatively compared to their building blocks. First, condensation in an isolated pore (cavity or constriction) with a significant amount of disorder is nucleated at a lower pressure than predicted by the Kelvin equation because of local pore heterogeneities that

catalyze condensation. Condensation and evaporation in any pore section of a complex pore structure are independent of boundary conditions if there is direct access to the gas reservoir. However, without direct access to the gas reservoir (i.e., ink-bottle geometry), the blocked cavity behaves differently. In this special case, condensation occurs at higher relative vapor pressures. We propose that a local minimum in the free energy is achieved when the cavity is blocked, slowing down the relaxation of adsorption to the global equilibrium. Because of these very slow dynamics, the local heterogeneities in the blocked cavity do not play a role and condensation is thus governed by the existing hemispherical meniscus at the constriction, following the Kelvin equation. The evaporation process in the blocked cavity is governed by pore blocking and/or cavitation. These experimental observations impose important limitations on studies of the role of pore morphology in capillary condensation.

AUTHOR INFORMATION

Corresponding Author

*E-mail: f.casanova@nanogune.eu.

Notes

The authors declare no competing financial interest.

ACKNOWLEDGMENTS

The financial support of the **Air Force Office of Scientific Research** is gratefully acknowledged. F.C. acknowledges financial support from the Spanish MEC and the Fulbright Commission. C.E.C. and A.M.R. acknowledge the California Space Grant Consortium (CASGC) for a Space Grant fellowship at the University of California—San Diego. A.M.R. thanks the University of California—San Diego for a Graduate Assistantship in Areas of National Need (GAANN) fellowship.

REFERENCES

- (1) Pacholski, C.; Sartor, M.; Sailor, M. J.; Cunin, F.; Miskelly, G. M. Biosensing using porous silicon double-layer interferometers: reflective interferometric Fourier transform spectroscopy. *J. Am. Chem. Soc.* **2005**, *127*, 11636–11645.
- (2) King, B. H.; Ruminski, A. M.; Snyder, J. L.; Sailor, M. J. Optical-fiber-mounted porous silicon photonic crystals for sensing organic vapor breakthrough in activated carbon. *Adv. Mater.* **2007**, *19*, 4530–4534.
- (3) Li, C. P.; Roshchin, I. V.; Batlle, X.; Viret, M.; Ott, F.; Schuller, I. K. Fabrication and structural characterization of highly ordered sub-100-nm planar magnetic nanodot arrays over 1 cm² coverage area. *J. Appl. Phys.* **2006**, *100*, 074318.
- (4) Gelb, L. D.; Gubbins, K. E.; Radhakrishnan, R.; Sliwinski-Bartkowiak, M. Phase separation in confined systems. *Rep. Prog. Phys.* **1999**, *62*, 1573–1659.
- (5) Iwamoto, S.; Saito, K.; Inoue, M.; Kagawa, K. Preparation of the xerogels of nanocrystalline titanias by the removal of the glycol at the reaction temperature after the glycothermal method and their enhanced photocatalytic activities. *Nano Lett.* **2001**, *1*, 417–421.
- (6) Valiullin, R.; Naumov, S.; Galvosas, P.; Karger, J.; Woo, H. J.; Porcheron, F.; Monson, P. A. Exploration of molecular dynamics during transient sorption of fluids in mesoporous materials. *Nature* **2006**, *443*, 965–968.
- (7) Stevens, W. J. J.; Lebeau, K.; Mertens, M.; Van Tendeloo, G.; Cool, P.; Vansant, E. F. Investigation of the morphology of the mesoporous SBA-16 and SBA-15 materials. *J. Phys. Chem. B* **2006**, *110*, 9183–9187.
- (8) Alvine, K. J.; Shpyrko, O. G.; Pershan, P. S.; Shin, K.; Russell, T. P. Capillary filling of anodized alumina nanopore arrays. *Phys. Rev. Lett.* **2006**, *97*, 175503.
- (9) Casanova, F.; Chiang, C. E.; Li, C. P.; Roshchin, I. V.; Ruminski, A. M.; Sailor, M. J.; Schuller, I. K. Effect of surface interactions on the hysteresis of capillary condensation in nanopores. *Europhys. Lett.* **2008**, *81*, 26003.
- (10) Casanova, F.; Chiang, C. E.; Li, C. P.; Roshchin, I. V.; Ruminski, A. M.; Sailor, M. J.; Schuller, I. K. Gas adsorption and capillary condensation in nanoporous alumina films. *Nanotechnology* **2008**, *19*, 315709.
- (11) Neimark, A. V.; Ravikovitch, P. I.; Grun, M.; Schuth, F.; Unger, K. K. Pore size analysis of MCM-41 type adsorbents by means of nitrogen and argon adsorption. *J. Colloid Interface Sci.* **1998**, *207*, 159–169.
- (12) Gregg, S. J.; Sing, K. S. W. *Adsorption, Surface Area, And Porosity*. Academic Press: London, 1982; pp 111–194.
- (13) Cordero, S.; Rojas, F.; Kornhauser, I.; Esparza, M.; Zgrablich, G. Menisci interactions during adsorption on mesoporous materials: Evaluation of delayed and advanced adsorption. *Adsorption* **2005**, *11*, 91–96.
- (14) Coasne, B.; Grosman, A.; Ortega, C.; Simon, M. Adsorption in noninterconnected pores open at one or at both ends: a reconsideration of the origin of the hysteresis phenomenon. *Phys. Rev. Lett.* **2002**, *88*, 256102.
- (15) Ravikovitch, P. I.; Neimark, A. V. Experimental confirmation of different mechanisms of evaporation from ink-bottle type pores: equilibrium, pore blocking, and cavitation. *Langmuir* **2002**, *18*, 9830–9837.
- (16) Puibasset, J. Adsorption/desorption hysteresis of simple fluids confined in realistic heterogeneous silica mesopores of micrometric length: a new analysis exploiting a multiscale Monte Carlo approach. *J. Chem. Phys.* **2007**, *127*, 154701.
- (17) Puibasset, J. Monte-Carlo multiscale simulation study of argon adsorption/desorption hysteresis in mesoporous heterogeneous tubular pores like MCM-41 or oxidized porous silicon. *Langmuir* **2009**, *25*, 903–911.
- (18) Naumov, S.; Khokhlov, A.; Valiullin, R.; Karger, J.; Monson, P. A. Understanding capillary condensation and hysteresis in porous silicon: network effects within independent pores. *Phys. Rev. E* **2008**, *78*, 060601.
- (19) Naumov, S.; Valiullin, R.; Kärger, J.; Monson, P. A. Understanding adsorption and desorption processes in mesoporous materials with independent disordered channels. *Phys. Rev. E* **2009**, *80*, 031607.
- (20) Coasne, B.; Di Renzo, F.; Galarneau, A.; Pellenq, R. J. M. Adsorption of simple fluid on silica surface and nanopore: Effect of surface chemistry and pore shape. *Langmuir* **2008**, *24*, 7285–7293.
- (21) Coasne, B.; Galarneau, A.; Di Renzo, F.; Pellenq, R. J. M. Effect of morphological defects on gas adsorption in nanoporous silicas. *J. Phys. Chem. C* **2007**, *111*, 15759–15770.
- (22) Grosman, A.; Ortega, C. Capillary condensation in porous materials. Hysteresis and interaction mechanism without pore blocking/percolation process. *Langmuir* **2008**, *24*, 3977–3986.
- (23) Wallacher, D.; Kunzner, N.; Kovalev, D.; Knorr, N.; Knorr, K. Capillary condensation in linear mesopores of different shape. *Phys. Rev. Lett.* **2004**, *92*, 195704.
- (24) Casanova, F.; Chiang, C. E.; Li, C. P.; Schuller, I. K. Direct observation of cooperative effects in capillary condensation: the hysteretic origin. *Appl. Phys. Lett.* **2007**, *91*, 243103.
- (25) Morishige, K.; Tateishi, N. Adsorption hysteresis in ink-bottle pore. *J. Chem. Phys.* **2003**, *119*, 2301–2306.
- (26) Grosman, A.; Ortega, C. Cavitation in metastable fluids confined to linear mesopores. *Langmuir* **2011**, *27*, 2364–2374.
- (27) Bruschi, L.; Mistura, G.; Liu, L.; Lee, W.; Gösele, U.; Coasne, B. Capillary condensation and evaporation in alumina nanopores with controlled modulations. *Langmuir* **2010**, *26*, 11894–11898.
- (28) Cordero, S.; Rojas, F.; Kornhauser, I.; Dominguez, A.; Vidales, A. M.; Lopez, R.; Zgrablich, G.; Riccardo, J. L. Pore-blocking and pore-assisting factors during capillary condensation and evaporation. *Appl. Surf. Sci.* **2002**, *196*, 224–238.

- (29) Vishnyakov, A.; Neimark, A. V. Monte Carlo simulation test of pore blocking effects. *Langmuir* **2003**, *19*, 3240–3247.
- (30) Sailor, M. J. *Porous Silicon in Practice*; Wiley-VCH: Weinheim, Germany, 2011.
- (31) Binder, M.; Edelman, T.; Metzger, T. H.; Peisl, J. Structure and correlations in porous silicon studied by X-ray scattering methods. *Solid State Commun.* **1996**, *100*, 13–16.
- (32) McLeod, H. A. *Thin-Film Optical Filters*; Bristol, U.K., 1986; p 49.
- (33) Jayannavar, A. M.; Kumar, N. Generalization of Bruggeman unsymmetrical effective-medium theory to a 3-component composite. *Phys. Rev. B* **1991**, *44*, 12014–12015.
- (34) Cohan, L. H. Sorption hysteresis and the vapor pressure of concave surfaces. *J. Am. Chem. Soc.* **1938**, *60*, 433–435.
- (35) Thommes, M.; Smarsly, B.; Groenewolt, M.; Ravikovitch, P. I.; Neimark, A. V. Adsorption hysteresis of nitrogen and argon in pore networks and characterization of novel micro- and mesoporous silicas. *Langmuir* **2006**, *22*, 756–764.